Tribology Letters (2020) 68:9
https://doi.org/10.1007/s11249-019-1246-8

ORIGINAL PAPER

The Relation Between Subsurface Stresses and Useful Wear Life in Sliding Contacts

Hossein Fereidouni[1] · Saleh Akbarzadeh[1] · M. M. Khonsari[2]

Received: 27 August 2019 / Accepted: 12 November 2019 / Published online: 2 December 2019

Abstract

Equations for quantifying the subsurface shear stress in dry point contact are utilized to obtain the value and location of the maximum subsurface shear stress. A series of experiments using a pin-on-disk tribometer is conducted on run-in specimens made of steel, brass, and aluminum, and the weight loss and wear rate of the specimen are measured. The results reveal a correlation between the depth of the maximum subsurface shear stress obtained from the model and the measured wear rate. It is shown that at the onset of failure, the friction coefficient suddenly increases. This increase affects the location of maximum subsurface shear stress by pushing it toward the surface and producing wear particles. SEM images of all three friction-pair tested reveal that the size of the wear particles is directly related to the applied load.

Graphical abstract

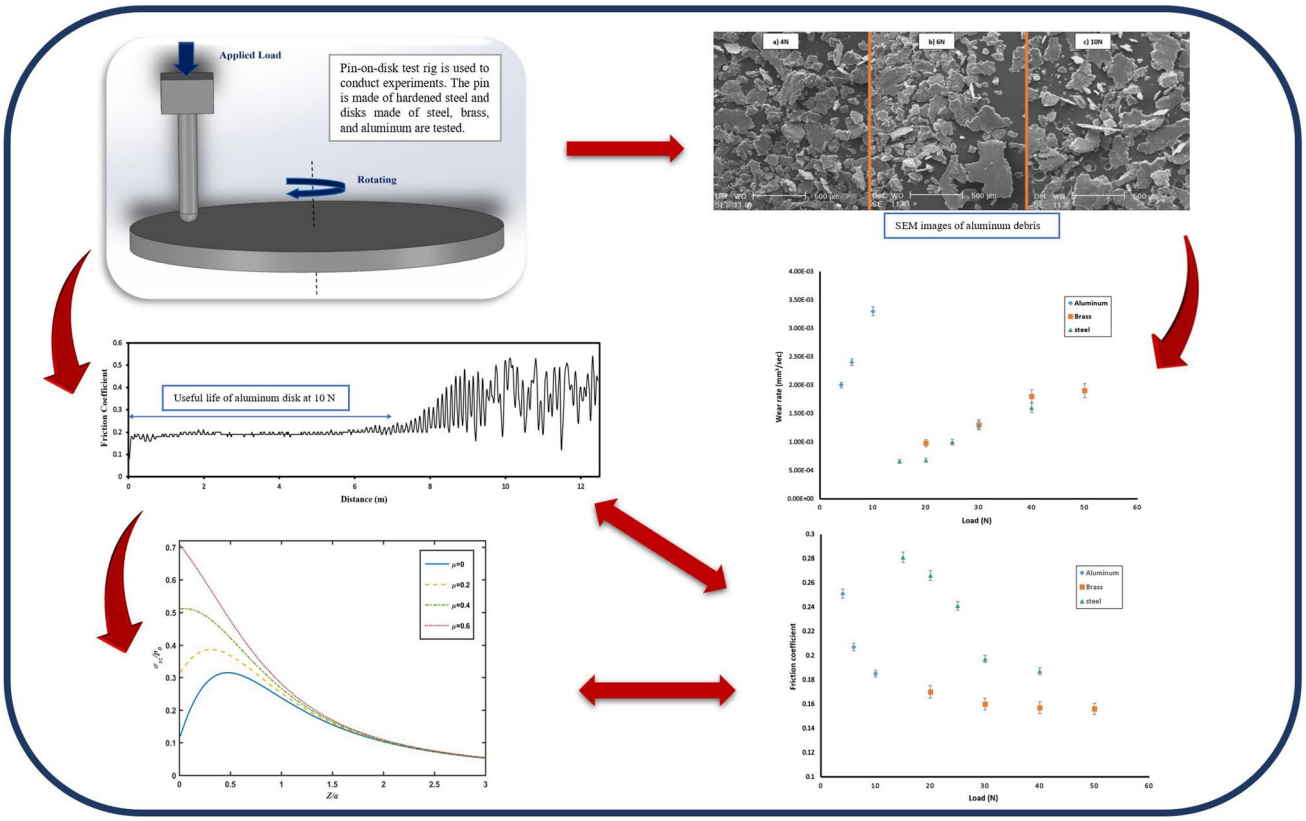

Keywords Wear · Subsurface stress · Friction coefficient · Pin-on-disk test

Extended author information available on the last page of the article

1 Introduction

Mechanical components are susceptible to wear when subjected to sliding and rolling contact. Wear manifests itself as a surface issue where wear particles are observed to detach themselves from the surface of the contacting bodies. But the origin of the wear lies below the surface where the microvoids and microcracks join and form subsurface cracks and travel toward the surface. Wear is affected by a multitude of operational and geometrical factors such as load, relative velocity, surface roughness, and environmental conditions like temperature. Therefore, numerous wear models have been developed to describe the material degradation during sliding contacts such as adhesive [1], abrasive [2], and delamination wear [3].

Regardless, akin to problems commonly encountered in fatigue, repetition of sliding tends to increase the accumulation of damage as a function of time. To this end, application of the cumulative fatigue damage model of Miner's rule [4] to predict the useful life in adhesive wear was recently investigated [5]. In sliding contacts, maximum subsurface shear stress is known to play an important role in the initiation of cracks and eventual fatigue [6–8]. It is observed that failure occurs when subsurface shear stress reaches a critical value in a certain location from the contact surface [9].

Given the importance of the subject, rich volumes of analytical and numerical solutions for the distribution of stress and strain in the contact zone have been reported. Johnson [10] derived the governing equations for calculation of subsurface stresses at any point under the contact surface in a two-dimensional elastic model subjected to normal and tangential loading. Vazquez et al. [11] presented a new method to directly and explicitly calculate the subsurface stress field in plane contacts. This model was based on Muskhelishvili complex potential [12] in which surface stress distribution is known for isotropic elastic contacting bodies and can be modeled as elastic half-planes. Using the Airy stress function, an analytical solution for calculation of subsurface stresses in a semi-infinite elastic model by Fourier series is presented by Chidlow et al. [13, 14]. Hamilton and Goodman [15] presented the complete elastic stress field for the sliding bodies that are exposed to both normal and tangential loading. Later, Hanson and Johnson [16] modified the elastic field for spherical Hertzian contact of isotropic bodies and provided alternative expressions. Analytical and numerical methods are also employed to assess the subsurface stresses in two and three-dimensional anisotropic contact [17]. Bray and Tang [18] experimentally quantified the subsurface stresses in steel plates and bars using ultrasonic waves. Techniques of high-resolution electron backscatter diffraction and finite element modeling are employed to calculate the subsurface stresses in the nickel single crystal [19]. Anoop et al. [20] utilized a numerical approach to evaluate the subsurface stress field under elastohydrodynamic line contact for bearing steel with retained austenite.

The effect of friction coefficient on the location of maximum subsurface stresses has been investigated before. In this study, the useful wear life of a sample experiencing sliding contact is determined. This useful life is measured by focusing on the variation of friction coefficient during the sliding time. The rapid rise in the friction coefficient is the sign for failure of the disk. The relation between this useful life and the maximum subsurface shear stress is studied. Pin-on-disk experiments are conducted under different applied loads. The useful life of the specimen in each case is determined and the evolution of maximum subsurface shear stress during testing is studied.

2 Theory

In general, the contact of most mechanical elements occurs in either cylindrical or spherical contact. Appendix presents the associated equations for determining their respective subsurface stresses. These equations correspond to the cases with and without shear loading.

To examine the characteristics of subsurface shear stresses, equations were simulated for the contact of two bodies made of stainless steel with an equivalent modulus of elasticity of $E = 200$ GPa and the Poisson ratio of $\upsilon = 0.28$. Figures 1 and 2 show the variation of subsurface stresses as a function of depth in the case that no shear loading exists for the cylindrical and spherical contact, respectively. The variation of these stresses in the case that shear loading exists is presented in Figs. 3 and 4.

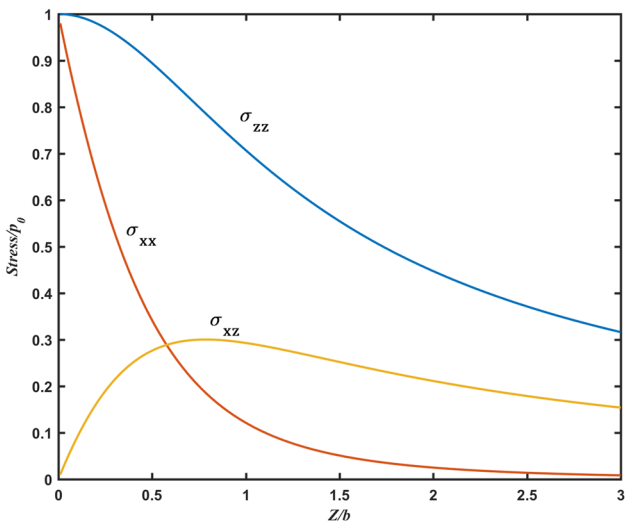

Fig. 1 Subsurface stresses corresponding to distance from surface in the cylindrical contact

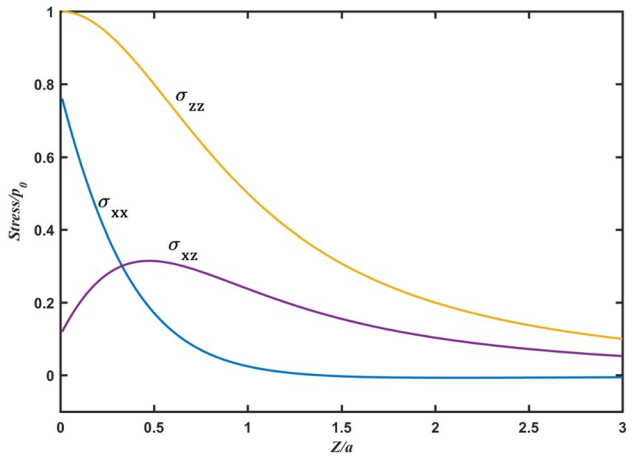

Fig. 2 Subsurface stresses corresponding to distance from surface in the spherical contact

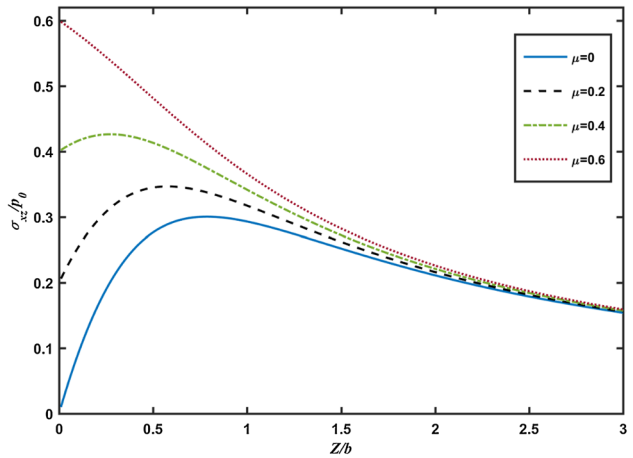

Fig. 3 Comparison of Subsurface shear stresses with different friction coefficient in the cylindrical contact

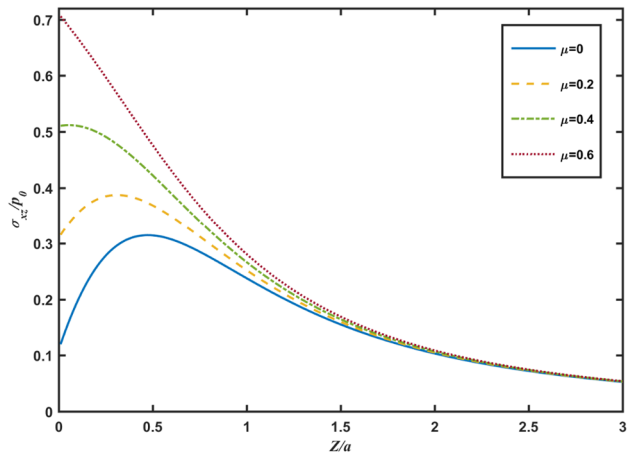

Fig. 4 Comparison of Subsurface shear stresses with different friction coefficient in the spherical contact

Examination of Figs. 1 and 2 indicates that the subsurface stresses in the cylindrical and point contact have similar trends. In both configurations, the subsurface shear stress experiences a maximum value at a specific depth below the surface. In spherical contact, unlike the cylindrical case, the subsurface shear stress does not start from zero and has a nonzero value at the contacting surface.

We now turn our attention to the effect of the friction coefficient on the subsurface stresses. As expected, in both types of contact, friction coefficient has no effect on σ_{xx} and σ_{zz}. However, as shown in Figs. 3 and 4, the subsurface shear stress varies significantly with the friction coefficient. Referring to Fig. 3, it can be seen that in cylindrical contact, increasing the friction coefficient causes the

Table 1 Effect of Friction coefficient on the location of maximum subsurface shear stress in cylindrical contact

Friction coefficient (μ)	(Z/b)
0.0	0.79
0.1	0.69
0.2	0.58
0.3	0.44
0.4	0.27
0.5	0.01
0.6	0.00

Table 2 Effect of Friction coefficient on the location of maximum subsurface shear stress in spherical contact

Friction coefficient (μ)	(Z/a)
0.0	0.47
0.1	0.40
0.2	0.31
0.3	0.20
0.4	0.05
0.5	0.00
0.6	0.00

Table 3 Material properties of pin and disk

Material/property	Pin		Disks	
	Steel	Steel st 37	Brass	Aluminum
H Hardness (BHN)	800	156	113	122
E Modulus of elasticity (GPa)	220	195	97	69
ν Poisson's ratio	0.26	0.28	0.31	0.33
ρ Density (kg/m^3)	7800	7800	8490	2810

Table 4 Pin and the disk dimensions

Pin			Disk	
Length	Diameter	Head radius	Diameter	Thickness
50 mm	5 mm	17 mm	50 mm	5 mm

location of the maximum shear stress to move closer to the contact surface. To better illustrate this result, the ratio of the distance from the surface to the contact half-width (Z/b) for maximum subsurface shear stress is calculated for different coefficients of friction and is shown in Table 1. It can be seen that in cylindrical contact for $\mu > 0.50$ the maximum shear stress occurs at the contact surface.

Figure 4 presents the influence of the friction coefficient on subsurface shear stress for spherical contact. It shows that in the absence of friction coefficient, the ratio of the distance from the surface to contact radius (Z/a) for the maximum subsurface shear stress is 0.47. An increase in the friction coefficient results in the movement of the location of maximum subsurface shear stress toward the surface. This trend is clearly shown in Table 2.

3 Experiments

In the previous section, it was shown that the subsurface shear stresses are a function of friction coefficient. In this section, a series of wear experiments are conducted to experimentally study the effect of maximum subsurface shear stress on the wear. The experiments are conducted using a pin-on-disk test rig. The mechanical properties of the pin and the disk are shown in Table 3. The pin is made of hardened steel, and disks made of steel, brass, and aluminum are tested. According to the hardness values of pin and disks reported in Table 3, the disks which are softer will experience adhesive wear. Surfaces of the disks are ground and have an average of asperity heights of $R_a = 0.1$ µm. In each test, a new pin is used. The dimensions of the pin and disks are given in Table 4. The pin is stationary and the disk rotates by the angular velocity of 50 rpm and rotating radius of 19 mm. In order to remove the transient effects, all the disks are run-in under the light load for a small sliding distance before each experiment. The duration of running-in was determined by examining the friction coefficient, which varies with time and becomes steady when the surfaces are run-in [5, 21].

During each experiment, a load cell attached to the data acquisition board measures the friction force and the software reports the friction coefficient as the ratio of the measured friction force to the normal load. A digital scale with

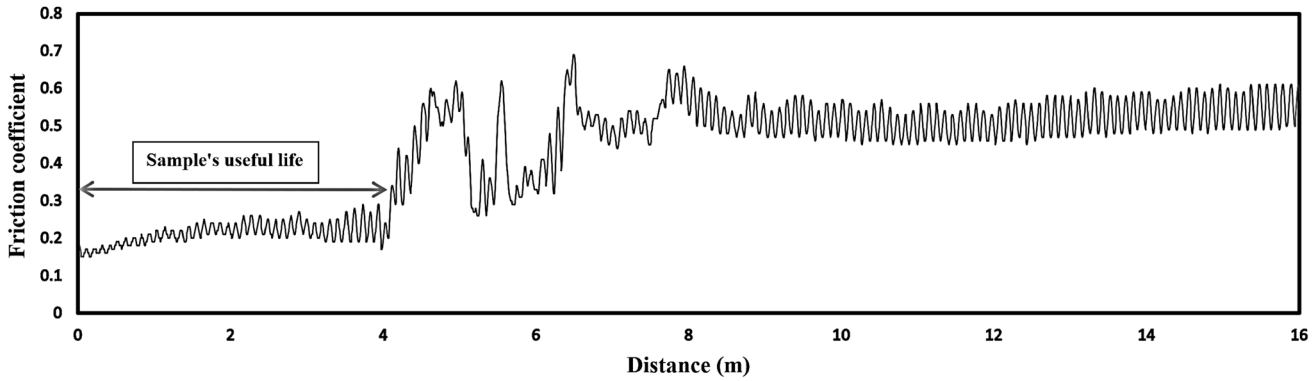

Fig. 5 Useful life of steel disk at 40 N

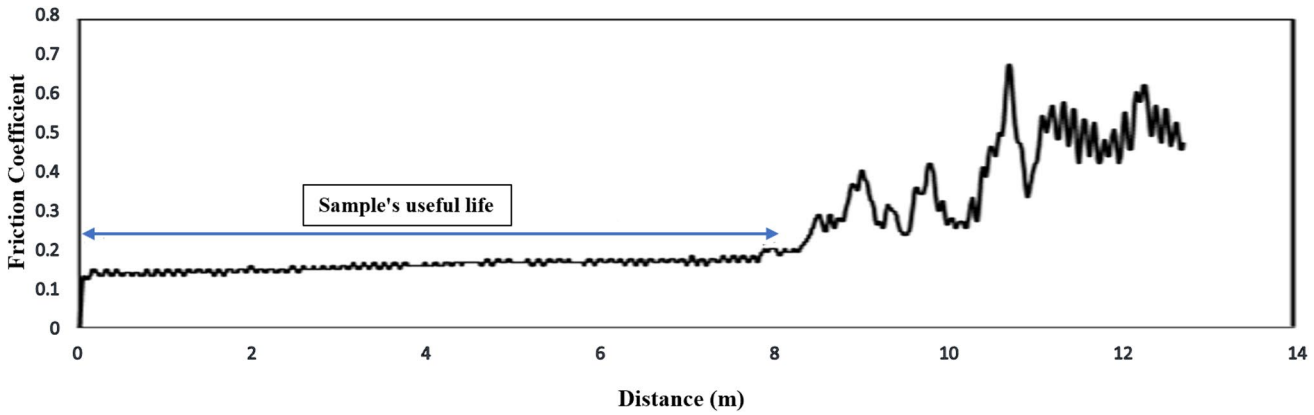

Fig. 6 Useful life of steel disk at 30 N

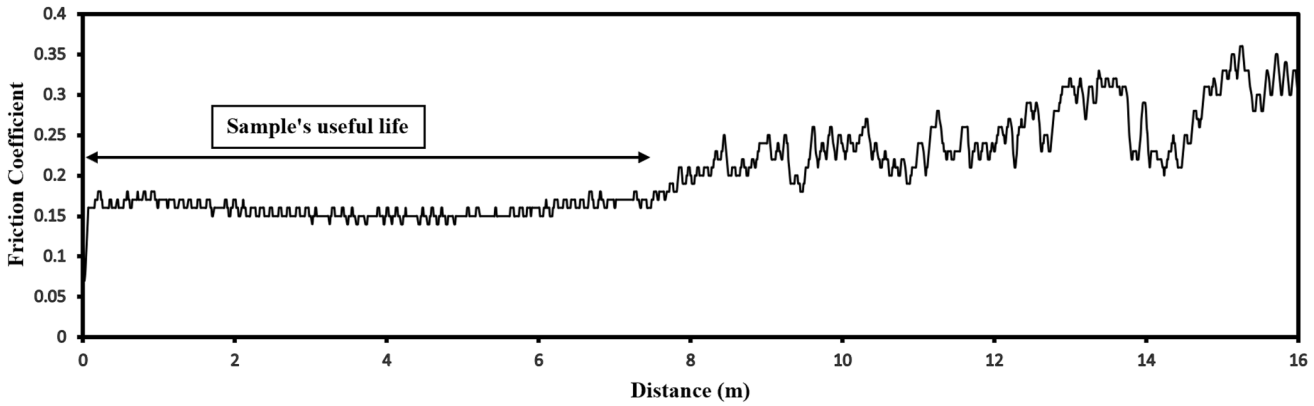

Fig. 7 Useful life of brass disk at 50 N

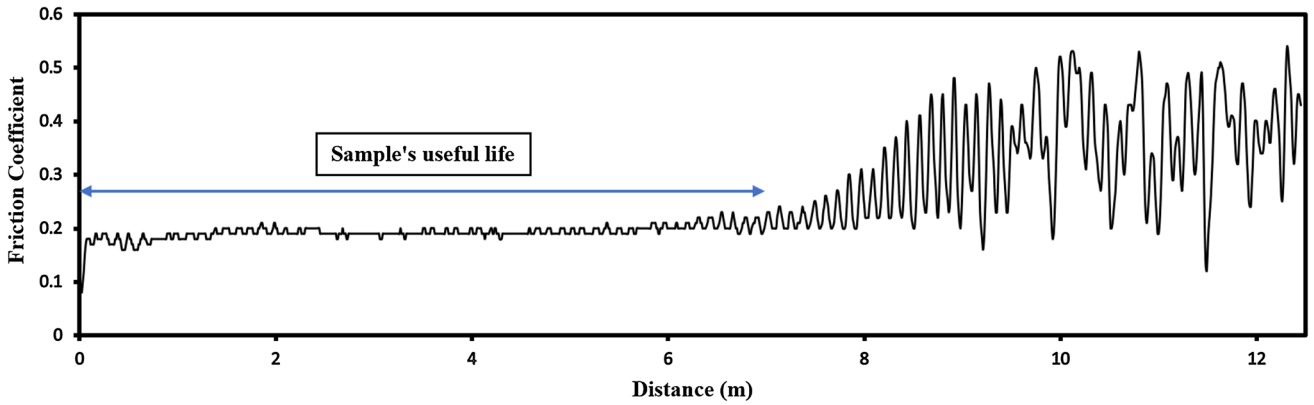

Fig. 8 Useful life of aluminum disk at 10 N

Table 5 Subsurface stresses and depth at which the maximum shear stress occurs under the constant speed of 0.1 m/s for the experiments with steel disk

Applied load (N)	Average of friction coefficient	a (mm)	σ_{xz}^{sp} (MPa)	Z_{max} (mm)	Weight loss (g)	Sliding distance (m)	Wear rate mm^3/s
15	0.285	0.120	215	2.63×10^{-2}	0.0006	11.5	6.6×10^{-4}
20	0.266	0.132	231	3.29×10^{-2}	0.0006	10	7.7×10^{-4}
25	0.241	0.142	241	3.83×10^{-2}	0.0007	8.5	1.0×10^{-3}
30	0.197	0.151	243	4.67×10^{-2}	0.0007	7	1.3×10^{-3}
40	0.187	0.166	264	5.31×10^{-2}	0.0005	4	1.6×10^{-3}

Table 6 Subsurface stresses and depth at which the maximum shear stress occurs under the constant speed of 0.1 m/s for the experiments with brass disk

Applied load (N)	Average of friction coefficient	a (mm)	σ_{xz}^{sp} (MPa)	Z_{max} (mm)	Weight loss (g)	Sliding distance (m)	Wear rate mm^3/s
20	0.170	0.151	152	5.29×10^{-2}	0.0010	12	9.8×10^{-4}
30	0.160	0.173	172	6.23×10^{-2}	0.0011	10	1.3×10^{-3}
40	0.157	0.191	189	6.86×10^{-2}	0.0012	8.5	1.8×10^{-3}
50	0.155	0.205	204	7.39×10^{-2}	0.0011	6.5	1.9×10^{-3}

Table 7 Subsurface stresses and depth at which the maximum shear stress occurs under the constant speed of 0.1 m/s for the experiments with aluminum disk

Applied load (N)	Average of friction coefficient	a (mm)	σ_{xz}^{sp} (MPa)	Z_{max} (mm)	Weight loss (g)	Sliding distance (m)	Wear rate mm^3/s
4	0.251	0.096	83	2.68×10^{-2}	0.0007	12	2.0×10^{-3}
6	0.207	0.109	90	3.41×10^{-2}	0.0006	9	2.4×10^{-3}
10	0.185	0.130	104	4.41×10^{-2}	0.0006	7	3.3×10^{-3}

an accuracy of 10^{-4} g is used to measure the weight loss of specimens before and after each experiment and quantify the weight loss.

Experiments are then conducted at different loads. In each case, the experiment is continued until the disk reaches the end of its useful life according to the following criterion. The point at which the friction coefficient starts to unstably increase is considered to signify the failure point and distance from the beginning of the test to the failure point is the disk's useful life [5, 21–23]. Figure 5 illustrates an example of the useful life for a steel disk subjected to 40 N load sliding at 0.1 m/s. After a continuous travel distance of 4 m, the friction coefficient became unstable, signaling the end of useful life. Figure 6 shows the same experiment with a pristine disk and a new pin subjected to a reduced load of 30 N. Results reveal that the useful life is inversely proportional to the force applied.

Figures 7 and 8 show the variation of friction coefficient versus sliding distance for brass and aluminum, respectively.

The pin-on-disk geometrical configuration can be represented by a sphere ($R_1 = 17$ mm) contacting a flat plate ($R_2 = \infty$). Tables 5, 6, and 7 report the calculated values of the radius of the contact patch, the Hertzian stress σ_{zz}^{sp}, the maximum subsurface shear stress, and the depth at which it occurs under different normal loads for steel, brass, and aluminum disks. The second column in Tables 5, 6, and 7 is the average friction coefficient obtained experimentally. This value is obtained by calculating the average coefficient of friction up to the failure point.

The third column shows the Hertzian radius of contact. As the applied load increases, the Hertzian radius increases. The fourth column is the maximum subsurface shear stress. As the applied load increases, the value of the maximum subsurface shear stress increases as well. The next column shows the location at which the maximum subsurface stress occurs. Figure 4 reveals that as the friction coefficient increases, the location of maximum subsurface shear stress moves closer to the surface. The weight loss which is measured from the beginning of each experiment up to the failure point is also reported in the tables. The sliding distance or the useful life is also shown for each applied load. As the

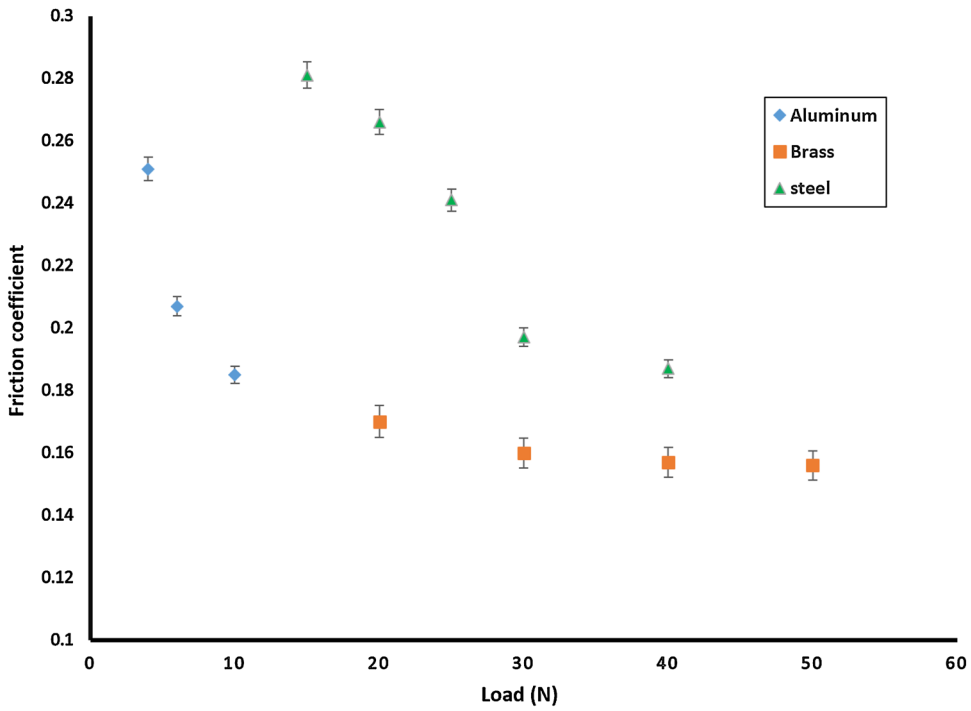

Fig. 9 Average of friction coefficient corresponding to the applied load

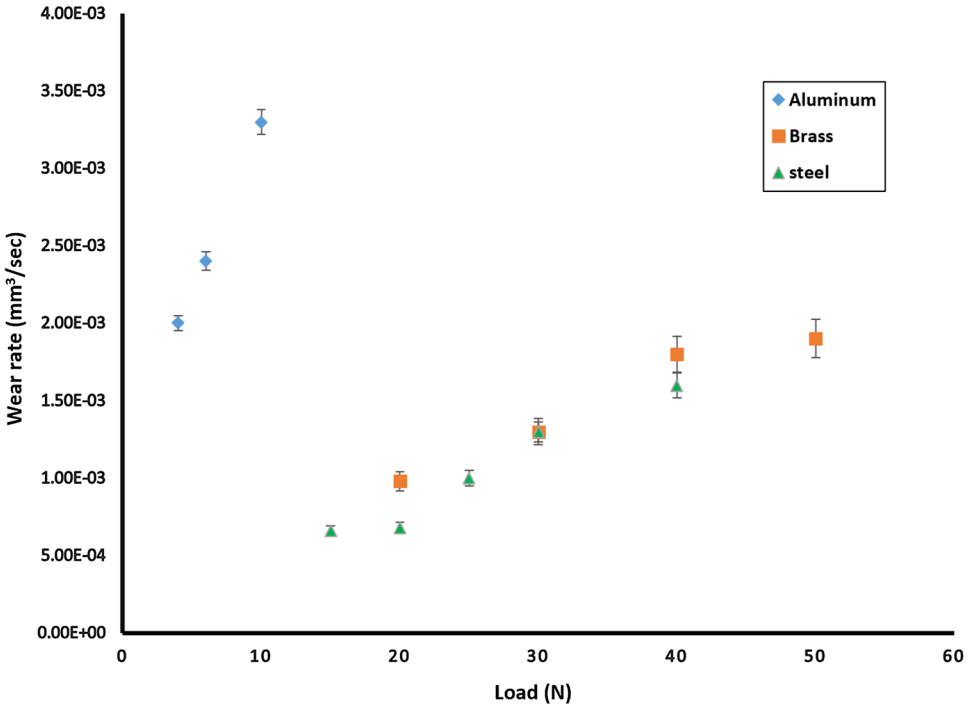

Fig. 10 Wear rate corresponding to the applied load

Table 8 Variation of wear depth for different loads under the constant speed of 0.1 m/s

Disk Material	Applied load (*N*)	Average of friction coefficient	*a* (mm)	Z_{max} (mm)	Weight loss (g)	Sliding distance (m)	Wear depth (μm)
Steel	15	0.285	0.120	2.63×10^{-2}	0.0006	11.5	2.8×10^{-2}
	20	0.266	0.132	3.29×10^{-2}	0.0006	10	2.9×10^{-2}
	25	0.241	0.142	3.83×10^{-2}	0.0007	8.5	3.7×10^{-2}
	30	0.197	0.151	4.67×10^{-2}	0.0007	7	4.2×10^{-2}
	40	0.187	0.166	5.31×10^{-2}	0.0005	4	4.8×10^{-2}
Brass	20	0.170	0.151	5.29×10^{-2}	0.0010	12	3.2×10^{-2}
	30	0.160	0.173	6.23×10^{-2}	0.0010	10	3.7×10^{-2}
	40	0.157	0.191	6.86×10^{-2}	0.0012	8.5	4.3×10^{-2}
	50	0.155	0.205	7.39×10^{-2}	0.0011	6.5	4.8×10^{-2}
Aluminum	4	0.251	0.096	2.68×10^{-2}	0.0007	12	10.8×10^{-2}
	6	0.207	0.109	3.41×10^{-2}	0.0006	9	10.9×10^{-2}
	10	0.185	0.130	4.41×10^{-2}	0.0006	7	11.7×10^{-2}

applied load increases, the sliding distance to the failure point or the useful life decreases.

Wear rate is calculated by dividing the weight loss to the sliding distance. According to the simulations and experimental results provided in Tables 5, 6, and 7, it is clear that increasing the applied load results in a decrease in the friction coefficient and an increase in the depth of maximum subsurface shear stress.

The reported weight loss is the loss in the weight of the disk from the beginning of the test up to the failure point. Therefore, with an increase in the applied load, the duration of the sliding distance to the point at which failure occurs decreases; hence, not much difference in the weight loss is seen. However, the wear rate increases with increasing the applied load. This can be concluded from the Archard's equation:

$$V = k\frac{Fd}{H} \tag{1}$$

where V is the worn volume, k is the Archard's wear coefficient, F is the applied load, d is the sliding distance, and H is the hardness of the softer material, i.e., the disk in this study. The relationship between the average friction

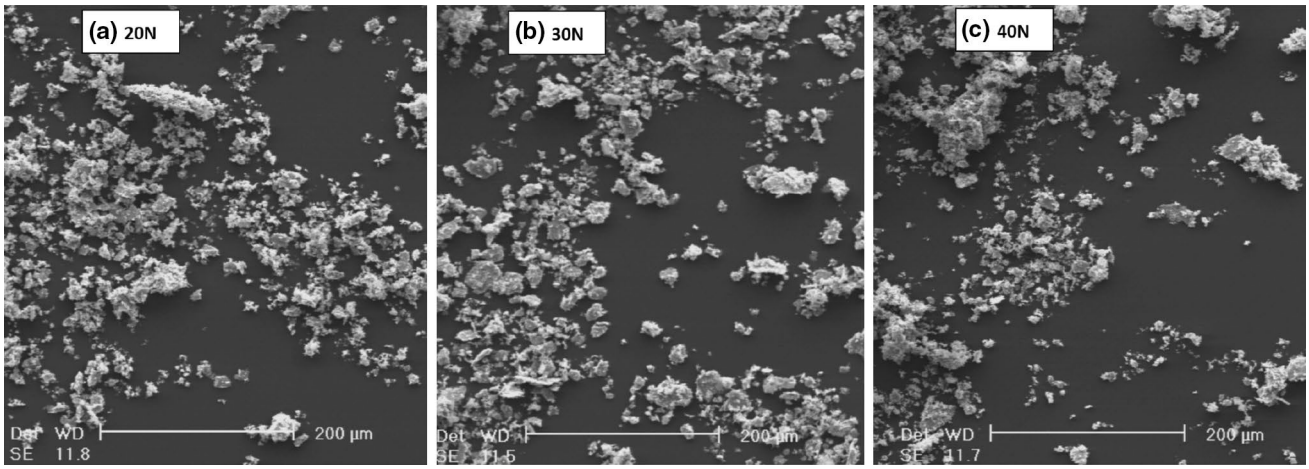

Fig. 11 SEM images for measuring wear particles of steel disk

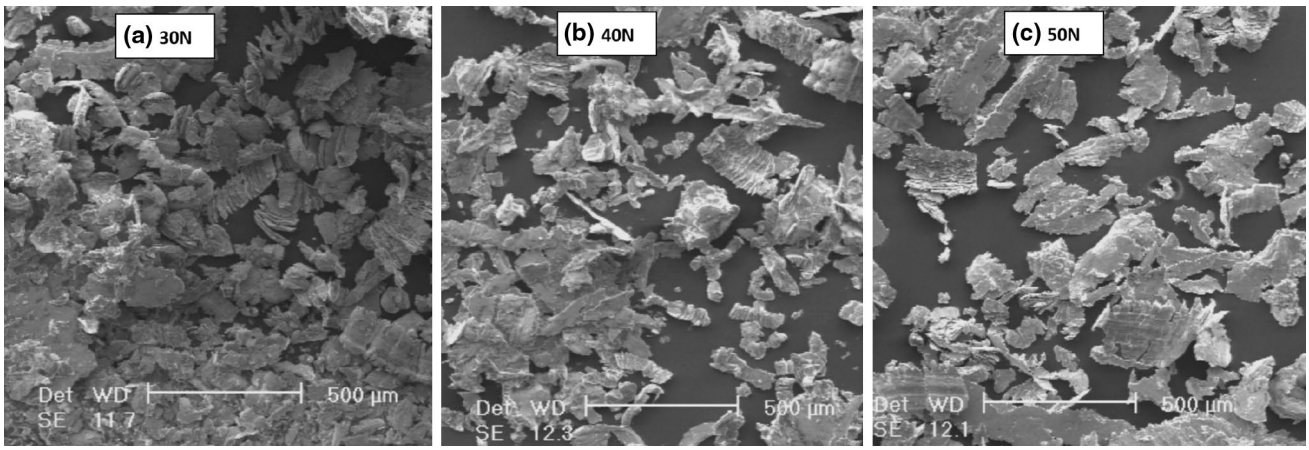

Fig. 12 SEM images for measuring wear particles of brass disk

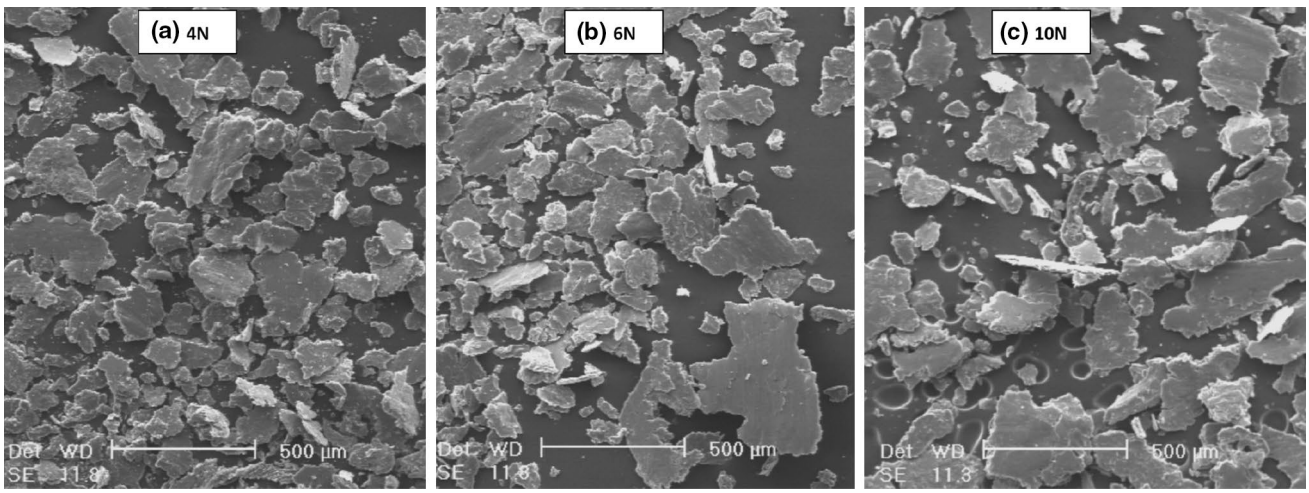

Fig. 13 SEM images for measuring wear particles of aluminum disk

Table 9 Average value of wear particles diameter

Material/applied load (*N*)	Steel			Brass			Auminum		
	20	30	40	30	40	50	4	6	10
Debris average diameter (μm)	3.84	3.95	4.02	12.33	13.48	13.92	13.53	14.27	15.57

coefficient and the applied load for all three types of disks is shown in Fig. 9. In this figure, it is clearly shown that in each case, increasing the applied load results in a decrease in the friction coefficient.

The relationship between the wear rate and applied load for all three types of disks is shown in Fig. 10. In each case, increasing the applied load results in an increase in the wear rate. The aluminum disk, with its lower density, experiences a higher wear rate compared to the steel and brass disks.

Another interesting point in these tests is the comparison of wear depth. The worn area is calculated by dividing the worn volume to the sliding distance. Table 8 shows the wear depth calculated from the ratio of the worn area to the Hertzian contact radius is reported as the wear depth. Since the experiments were conducted for a small duration of time, the wear depth has a small value.

As the applied load increases, the weight loss does not change significantly but the wear depth increases. Larger wear depth here means larger wear particles. Another way to translate this finding is that as the applied load increases, the friction coefficient decreases. Thus, the point of maximum subsurface shear stress moves further into the bulk of the rotating disk. At this stage, the value of the friction coefficient sharply increases in an unstable manner. This increase causes the subsurface cracks to move toward the disk surface. For the tests conducted under higher loads, these cracks travel a longer distance from inside the bulk toward the surface. Thus, once the location of the maximum subsurface shear stress reaches the surface, large particles of material are detached from the disk as wear particles. Therefore, the wear depth is larger.

In order to verify this finding, SEM images were taken from the disk surface to measure the average of wear particles. For different loads of 20 N, 30 N, and 40 N the images of debris for steel disk are shown in Fig. 11. In Fig. 12, the images of wear particle for brass disk for different loads of 30 N, 40 N, and 50 N are shown. For different loads of 4 N, 6 N, and 10 N, the images of debris for aluminum disk are shown in Fig. 13. Digital image processing was performed to measure the dimensions of the particles. A narrow film of wear particles prepared for scanning with an electronic microscope (Philips XL30 SEM) and ImageJ software was utilized to measure the average size of the wear particles. As shown in Table 9, the average size of the wear particles increases as the applied load increases.

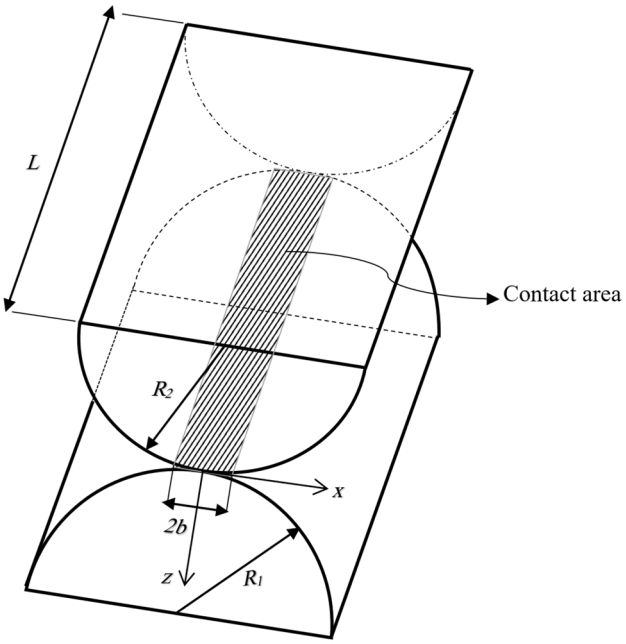

Fig. 14 Cylindrical contact

4 Conclusions

In this study, the effect of the applied load and the friction coefficient on the location of the maximum subsurface shear stress is studied. The magnitude of the maximum subsurface shear stress and the location where it occurs are functions of the applied load and the friction coefficient. These two factors have opposite effects on the location of maximum subsurface shear stress. Meaning that increasing the applied load results in an increase in the depth of maximum subsurface shear stress and an increase in the friction coefficient reduces this stress. It should be noted that the friction coefficient is a function of load, speed, properties of contacting materials, and surface roughness.

The useful life of a tribo-pair is evaluated using a pin-on-disk test apparatus with specimens made of steel, brass, and aluminum. In order to quantify the useful life, the friction coefficient between the contacting surfaces is carefully observed. The onset of failure is considered to be the point at which the friction coefficient experiences a rapid rise. It is found that as a result of this rapid rise in the friction coefficient, near the failure point, the location of the maximum subsurface shear stress moves toward the surface and results

in the formation of wear particles. Results also show that an increase in the applied load results in a decrease in the friction coefficient, moving the location of the maximum subsurface shear stress deeper into the surface. Thus, the higher the load, the deeper the location of the maximum subsurface shear stress and the longer the travel distance to the surface becomes. As a result, the size of the wear particles becomes larger with increasing the normal load. Examination of the SEM images of the wear debris for all the tested specimens confirms this finding.

Appendix

Governing Equations for Substress Field in Cylindrical and Spherical Contacts

Cylindrical Contact

A schematic view of the contact of two elastic cylindrically shaped bodies is shown in Fig. 14 in Appendix. The contact area of two cylinders is a rectangle of length L and width of $2b$. The half-width of b is given by [24]:

$$b=\sqrt{\frac{4F\left[\frac{1-v_1^2}{E_1}+\frac{1-v_2^2}{E_2}\right]}{\pi L\left(\frac{1}{R_1}+\frac{1}{R_2}\right)}} \tag{A1}$$

where E_1 and E_2 are moduli of elasticity, ν_1 and ν_2 are the Poisson's ratios for cylinders 1 and 2, respectively, and L is the length of the contact area.

The equations for calculation of subsurface stress in a half-space loaded by a normal pressure $p(s)$ and shear loading $q(s)$ are [10]:

$$\sigma_{xx}=-\frac{2z}{\pi}\int\frac{p(s)(x-s)^2\mathrm{d}s}{\left\{(x-s)^2+z^2\right\}^2}-\frac{2}{\pi}\int\frac{q(s)(x-s)^3\mathrm{d}s}{\left\{(x-s)^2+z^2\right\}^2} \tag{A2}$$

$$\sigma_{zz}=-\frac{2z^3}{\pi}\int\frac{p(s)\mathrm{d}s}{\left\{(x-s)^2+z^2\right\}^2}-\frac{2z^2}{\pi}\int\frac{q(s)(x-s)ds}{\left\{(x-s)^2+z^2\right\}^2} \tag{A3}$$

$$\tau_{xz}=-\frac{2z^2}{\pi}\int\frac{p(s)(x-s)ds}{\left\{(x-s)^2+z^2\right\}^2}-\frac{2z}{\pi}\int\frac{q(s)(x-s)^2\mathrm{d}s}{\left\{(x-s)^2+z^2\right\}^2} \tag{A4}$$

where for semi-elliptic pressure distribution in cylindrical contact, $p(s)$ and $q(s)$ are given by:

$$p(s)=\frac{2F}{\pi bL}\sqrt{1-\frac{(x-s)^2}{b^2}} \tag{A5}$$

$$q(s)=\frac{2\mu F}{\pi bL}\sqrt{1-\frac{(x-s)^2}{b^2}} \tag{A6}$$

where F is the applied load and μ is the friction coefficient. Maximum pressure $p_0=\frac{2F}{\pi bL}$ occurs at $x=0$.

By substituting Eqs. (A5) and (A6) into Eqs. (A2) to (A4) and integrating the results, the following expressions for the subsurface stresses are obtained:

$$\begin{aligned}\sigma_{xx}^{Cy}(x,z)=\frac{2F}{\pi bL}&\left[\frac{-2z}{\pi b}\sin^{-1}\left(\frac{s-x}{b}\right)+\frac{2z^2+b^2}{\pi b\sqrt{z^2+b^2}}\tan^{-1}\left(\frac{\sqrt{z^2+b^2}(s-x)}{bz\sqrt{1-\frac{(x-s)^2}{b^2}}}\right)-\frac{z(s-x)}{\pi\sqrt{1-\frac{(x-s)^2}{b^2}}\left(\frac{\left(z^2+b^2\right)(s-x)^2}{b^2\left(1-\frac{(x-s)^2}{b^2}\right)}+z^2\right)}\right]\Bigg|_{-b}^{b}\\&+\frac{2\mu F}{\pi bL}\left[\frac{\left(z^4+\left(-z^2-b^2\right)\left(2z^2+b^2\right)+2b^2z^2+b^4\right)\ln\left(\frac{\sqrt{b^2-(s-x)^2}+\sqrt{z^2+b^2}}{\left|\sqrt{b^2-(s-x)^2}-\sqrt{z^2+b^2}\right|}\right)}{2\pi b\sqrt{z^6+3b^2z^4+3b^4z^2+b^6}}-\frac{\left(2z^2+b^2\right)ln\left(\frac{\left|\sqrt{b^2-(s-x)^2}-\sqrt{z^2+b^2}\right|}{\sqrt{b^2-(s-x)^2}+\sqrt{z^2+b^2}}\right)}{\pi b\sqrt{z^2+b^2}}\right.\\&\left.+\frac{\left(-z^4-\left(-z^2-b^2\right)\left(2z^2+b^2\right)-2b^2z^2-b^4\right)}{2\pi b\left(z^2+b^2\right)\sqrt{b^2-(s-x)^2}+2\pi b\sqrt{\left(z^2+b^2\right)^3}}+\frac{\left(-z^4-\left(-z^2-b^2\right)\left(2z^2+b^2\right)-2b^2z^2-b^4\right)}{2\pi b\left(z^2+b^2\right)\sqrt{b^2-(s-x)^2}-2\pi b\sqrt{\left(z^2+b^2\right)^3}}-\frac{2\sqrt{b^2-(s-x)^2}}{\pi b}\right]\Bigg|_{-b}^{b}\end{aligned} \tag{A7}$$

$$\sigma_{zz}^{cy}=\frac{2F}{\pi bL}\left[-\frac{b}{\pi\sqrt{z^2+b^2}}\tan^{-1}\left(\frac{\sqrt{z^2+b^2}(s-x)}{bz\sqrt{1-\frac{(x-s)^2}{b^2}}}\right)-\frac{z(s-x)}{\pi\sqrt{1-\frac{(x-s)^2}{b^2}}\left(\frac{\left(z^2+b^2\right)(s-x)^2}{b^2\left(1-\frac{(x-s)^2}{b^2}\right)}+z^2\right)}\right]_{-b}^{b}$$
$$+\frac{2\mu F}{\pi bL}\left[\frac{z^2\left(z^2+b^2\right)\ln\left(\frac{\sqrt{b^2-(s-x)^2}+\sqrt{z^2+b^2}}{\left|\sqrt{b^2-(s-x)^2}-\sqrt{z^2+b^2}\right|}\right)}{2\pi b\sqrt{z^6+3b^2z^4+3b^4z^2+b^6}}+\frac{z^2ln\left(\frac{\left|\sqrt{b^2-(s-x)^2}-\sqrt{z^2+b^2}\right|}{\sqrt{b^2-(s-x)^2}+\sqrt{z^2+b^2}}\right)}{\pi b\sqrt{z^2+b^2}}-\frac{z^2}{2\pi b\left(\sqrt{b^2-(s-x)^2}+\sqrt{z^2+b^2}\right)}-\frac{z^2}{2\pi b(\sqrt{b^2-(s-x)^2}-\sqrt{z^2+b^2})}\right]_{-b}^{b} \tag{A8}$$

$$\sigma_{xz}^{cy}(x,z)=\frac{2F}{\pi bL}\left[-\frac{\sqrt{z^2+b^2}}{\pi b}\tan^{-1}\left(\frac{\sqrt{z^2+b^2}(s-x)}{bz\sqrt{1-\frac{(x-s)^2}{b^2}}}\right)+\frac{z}{\pi b}\sin^{-1}\left(\frac{s-x}{b}\right)\right]_{-b}^{b}$$
$$+\frac{2\mu F}{\pi bL}\left[\frac{-2z}{\pi b}\sin^{-1}\left(\frac{s-x}{b}\right)+\frac{2z^2+b^2}{\pi b\sqrt{z^2+b^2}}\tan^{-1}\left(\frac{\sqrt{z^2+b^2}(s-x)}{bz\sqrt{1-\frac{(x-s)^2}{b^2}}}\right)-\frac{z(s-x)}{\pi\sqrt{1-\frac{(x-s)^2}{b^2}}\left(\frac{\left(z^2+b^2\right)(s-x)^2}{b^2\left(1-\frac{(x-s)^2}{b^2}\right)}+z^2\right)}\right]_{-b}^{b} \tag{A9}$$

Spherical Contact

A general schematic of contact of two elastic bodies is illustrated in Fig. 15 in Appendix. The radius of the spherical contact area resulting in a semi-elliptic pressure distribution which is formed due to the applied loading is calculated from the theory of elasticity as [24]:

$$a=\sqrt[3]{\frac{3F\left[\frac{1-\upsilon_1^2}{E_1}+\frac{1-\upsilon_2^2}{E_2}\right]}{4\left(\frac{1}{R_1}+\frac{1}{R_2}\right)}} \tag{A10}$$

where E_1 and E_2 are moduli of elasticity for spheres 1 and 2 and ν_1 and ν_2 are the Poisson's ratios.

For the contact with a sphere on the flat plate, the flat plate is considered as a sphere with an infinitely large radius ($R_1=\infty$).

On the surface where $z=0$, the expression for pressure components reduces to the following.

$$P_{zz}=\frac{3F}{2\pi a^3}\sqrt{a^2-r^2} \tag{A11}$$

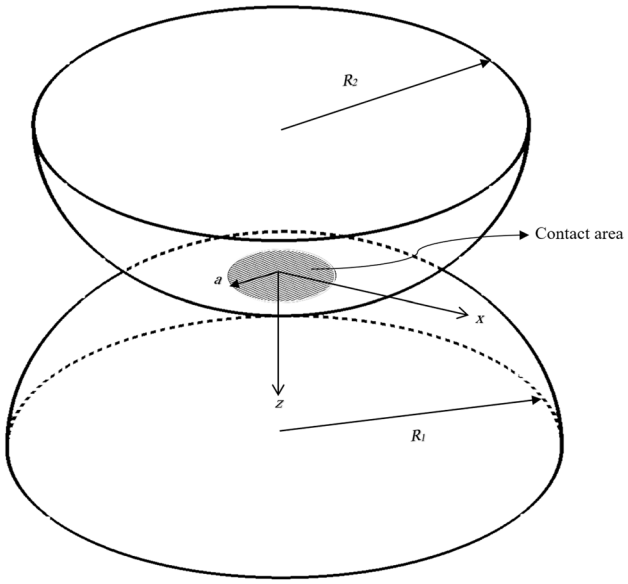

Fig. 15 Spherical contact

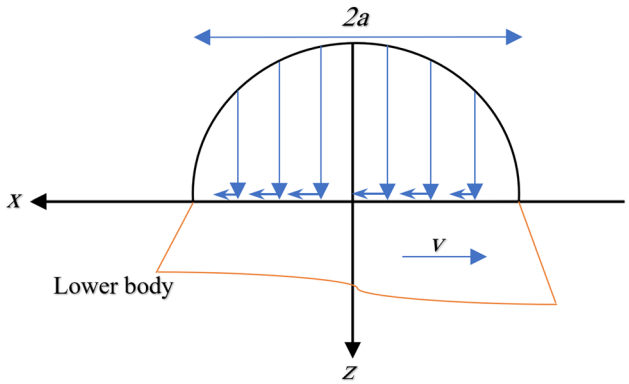

Fig. 16 Schematic view of pressure distribution in spherical contact

$$P_{xz} = \frac{3\mu F}{2\pi a^3}\sqrt{a^2 - r^2} \tag{A12}$$

$$r = \sqrt{x^2 + y^2} < a \tag{A13}$$

where μ is the friction coefficient, F is the applied load, and a is the contact radius. The maximum contact pressure $p_0 = \frac{3F}{2\pi a^2}$ occurs at the center of circular contact $r=0$. Figure 16 in Appendix shows a schematic view of the pressure distribution.

As a result of loading, subsurface stresses are created inside the contacting bodies. Subsurface stresses for spherical contact of isotropic bodies for normal loading are given by [16]:

$$\sigma_{xx} = \frac{3F}{2\pi a^3}\left[2(1+\upsilon)z\arcsin\left(\frac{J_1}{r}\right) - (1+2\upsilon)\sqrt{a^2 - {J_1}^2} - \frac{za\sqrt{{J_2}^2 - a^2}}{{J_2}^2 - {J_1}^2}\right] \tag{A14}$$

$$\sigma_{zz} = -\frac{3F}{2\pi a^3}\left[\frac{\sqrt[3]{(a^2 - {J_1}^2)^2}}{{J_2}^2 - {J_1}^2}\right] \tag{A15}$$

$$\sigma_{xz} = \left|\frac{\sigma_{zz} - \sigma_{xx}}{2}\right| \tag{A16}$$

where parameters of J_1 and J_3 are denoted as:

$$J_1 = \frac{1}{2}\left[\sqrt{(r+a)^2 + z^2} - \sqrt{(r-a)^2 + z^2}\right] \tag{A17}$$

$$J_2 = \frac{1}{2}\left[\sqrt{(r+a)^2 + z^2} + \sqrt{(r-a)^2 + z^2}\right] \tag{A18}$$

Subsurface stresses for spherical contact of isotropic bodies for shear loading are given by [16]:

$$\sigma'_{xx} = \frac{3F}{2\pi a^3}(\mu cos\theta)r\left[(1+\upsilon)\left(-\arcsin\left(\frac{J_1}{r}\right) + \frac{J_1}{r^2}\sqrt{r^2 - {J_1}^2}\right) + z{J_1}^2\frac{\sqrt{a^2 - {J_1}^2}}{r^2({J_2}^2 - {J_1}^2)}\right] \tag{A19}$$

$$\sigma'_{zz} = -\frac{3F}{2\pi a^3}(\mu cos\theta)\left[za^2 J_1\frac{\sqrt{{J_2}^2 - r^2}}{{J_2}^2({J_2}^2 - {J_1}^2)}\right] \tag{A20}$$

$$\sigma'_{xz} = \frac{3F}{4\pi a^3}\mu 3\arcsin\left(\frac{J_1}{r}\right) - 2\sqrt{a^2 - {J_1}^2} - za^2\frac{\sqrt{r^2 - {J_1}^2}}{{J_1}^2({J_2}^2 - {J_1}^2)} - e^{-2i\theta}z{J_1}^3\frac{\sqrt{r^2 - {J_1}^2}}{r^2({J_2}^2 - {J_1}^2)} \tag{A21}$$

where θ is the polar angle. In the case when a normal, as well as shear loading, is applied, the subsurface stresses are calculated as:

$$\sigma^{sp}_{xx} = \sigma_{xx} + \sigma'_{xx} \tag{A22}$$

$$\sigma^{sp}_{zz} = \sigma_{zz} + \sigma'_{zz} \tag{A23}$$

$$\sigma^{sp}_{xz} = \sigma_{xz} + \sigma'_{xz} \tag{A24}$$

References

1. Archard, J.: Contact and rubbing of flat surfaces. J. Appl. Phys. **24**(8), 981–988 (1953)
2. Khruschov, M.: Resistance of metals to wear by abrasion, as related to hardness. Proc. Conf, Lubrication and Wear, IME (1957)
3. Suh, N.P.: The delamination theory of wear. Wear **25**(1), 111–124 (1973)
4. Miner, M.: Cumulative fatigue damage. J Appl Mech **12**(3), A159–A164 (1945)
5. Akbarzadeh, S., Khonsari, M.M: On the applicability of Miner's rule to adhesive wear. Tribol. Lett. **63**(2):29 (2016)
6. Jalalahmadi, B., Sadeghi, F.: A Voronoi finite element study of fatigue life scatter in rolling contacts. J. Tribol. **131**(2), 022203 (2009)
7. Raje, N., et al.: A statistical damage mechanics model for subsurface initiated spalling in rolling contacts. J. Tribol. **130**(4), 042201 (2008)
8. Rosenfield, A.: A fracture mechanics approach to wear. Wear **61**(1), 125–132 (1980)
9. Beheshti, A., Khonsari, M.: On the prediction of fatigue crack initiation in rolling/sliding contacts with provision for loading sequence effect. Tribol. Int. **44**(12), 1620–1628 (2011)
10. Johnson, K.L., Johnson, K.L.: *Contact mechanics* (Cambridge University Press, Cambridge, 1987)
11. Vázquez, J., et al.: Explicit equations for sub-surface stress field in plane contacts. Int. J. Mech. Sci.**67**, 53–58 (2013)
12. Muskhelishvili, N.I.: *Some Basic Problems of the Mathematical Theory of Elasticity* (Springer, Dordrecht, 1977)
13. Chidlow, S., et al.: A solution method for the sub-surface stresses and local deflection of a semi-infinite inhomogeneous elastic medium. Appl. Math. Model. **36**(8), 3486–3501 (2012)
14. Chidlow, S., et al.: Predicting the deflection and sub-surface stress field within two-dimensional inhomogeneously elastic bonded layered solids under pressure. Int. J. Solids Struct .**48**(22–23), 3243–3256 (2011)
15. Hamilton, G., Goodman, L.: The stress field created by a circular sliding contact. J. Appl. Mech. **33**(2), 371–376 (1966)
16. Hanson, M., Johnson, T.: The elastic field for spherical Hertzian contact of isotropic bodies revisited: some alternative expressions. J. Tribol. **115**(2), 327–332 (1993)

17. Arakere, N.K., et al.: Subsurface stress fields in face-centered-cubic single-crystal anisotropic contacts. J. Eng. Gas Turbines Power **128**(4), 879–888 (2006)
18. Bray, D.E., Tang, W.: Subsurface stress evaluation in steel plates and bars using the LCR ultrasonic wave. Nucl. Eng. Des. **207**(2), 231–240 (2001)
19. Kartal, M., et al.: Determination of sub-surface stresses at inclusions in single crystal superalloy using HR-EBSD, crystal plasticity and inverse eigenstrain analysis. Int. J. Solids Struct. **67**, 27–39 (2015)
20. Anoop, A.D., et al.: Numerical evaluation of subsurface stress field under elastohydrodynamic line contact for AISI 52100 bearing steel with retained austenite. Wear **330–331**, 636–642 (2015)
21. Lijesh, K.P., Khonsari, M.M.: On the integrated degradation coefficient for adhesive wear: a thermodynamic approach. Wear **48**, 138–150 (2018)
22. Lijesh, K.P., Khonsari, M.M.: On the modeling of adhesive wear with consideration of loading sequence. Tribol. Lett. **66**, 13–23 (2018)
23. Fereidouni, H., Akbarzadeh, S., Khonsari, M.M.: On the assessment of variable loading in adhesive wear. Tribol. Int. **129**, 167–176 (2019)
24. Budynas, R.G., Nisbett, J.K.: *Shigley's Mechanical Engineering Design* (McGraw-Hill, New York, 2008)

Affiliations

Hossein Fereidouni[1] · Saleh Akbarzadeh[1] · M. M. Khonsari[2]

✉ M. M. Khonsari
khonsari@me.lsu.edu

[1] Department of Mechanical Engineering, Isfahan University of Technology, Isfahan 84156-83111, Iran

[2] Department of Mechanical and Industrial Engineering, Louisiana State University, Baton Rouge, LA 70803, USA